UAV survey method to Monitoring and analysing geological hazards: The Case study of mud volcano of Villaggio Santa Barbara, Caltanissetta (Sicily)

Fabio Brighenti[1], Francesco Carnemolla [1], Danilo Messina[3] & Giorgio De Guidi[1 2]

5 [1]Department of Biology, geology and Environmental Sciences, University of Catania, Catania, 95129, Corso Italia 55 – 57, Italy
[2]CRUST-Interuniversity Center for 3D Seismotectonics with territorial applications - UR-UniCT, Catania, 95129, Corso Italia 55 – 57, Italy
[3]Independent Researcher

10 *Correspondence to*: Giorgio De Guidi (deguidi@unict.it)

Abstract. All active geological processes determine effects on the soil due to different deformation processes: surface uplift and subsidence, shear lineaments with differential kinematics in relation to the source and the soils involved. Among all the active geological processes on Santa Barbara mud volcano (Caltanissetta town, Italy), represents a dangerous site because it caused, on 11 August 2008, a paroxysmal event, which determined severe damages to the infrastructures at around to 2 km

15 the paroxysmal event. The remote sensing of surface deformation now represents a key tool for the evaluation and monitoring of the hazard. The use of unmanned aerial vehicles (UAVs) in contexts of natural danger presents three main steps for risk assessment and monitoring: pre-post event data acquisition, emergency support and monitoring. Here we present a methodology for monitoring deformation processes that may be precursors of paroxysmal events on the Santa Barbara mud volcano. Among the precursors, the lifting and development of structural features are the most important, with

20 dimensions ranging from centimetre to decimetre. Therefore in relation to the magnitudes of the phenomena involved, the objective of this work is (going from the acquisition phase, to the SfM processing chain and the use of the M3C2-PM algorithm for the comparison between point clouds and uncertainty analysis with a statistical approach) the monitoring of deformation processes, with centimetre precision and a temporal frequency of 1 - 2 months, as precursor indications of hazard.

1 Introduction

The monitoring of active geological processes is a key preventive action in risk mitigation. Disasters occur when two factors - danger and vulnerability - coincide. The risk that a disaster occurs is proportional to the magnitude of the hazard and the vulnerability of the affected population. Among the deformation monitoring systems, the photogrammetry technique from

30 unmanned aerial vehicles (UAVs) is spreading thanks to the high efficiency in data acquisition, the low cost compared to

traditional techniques and in the acquisition of high resolution images (Fonstad et al., 2013; Harwin and Lucieer, 2012; James and Robson, 2012; James et al., 2017/a/b; Javernick et al., 2013; Johnson et al., 2014; Westoby et al., 2012). This technique is important to study of catastrophic natural events such as floods, earthquakes, landslides, landslides, subsidence, etc. The different acquisition methods and the ability to obtain high spatial and temporal resolutions allow to obtain detailed

35 information on the evolution of the landscape. In this context, UAVs therefore offer unprecedented spatial and temporal resolution (Boccardo et al. 2015) and it is an effective and complementary tool for field investigations. Furthermore, UAVs have other advantages including: (i) the ability to fly at low altitudes, (ii) the ability to reach remote locations and capture high-resolution images, (iii) the ability to host multiple sensors (cameras, Lidar thermal imaging cameras, navigation / inertial sensors, etc.), (iv) the ability to capture images at different angles, and (v) the flexibility to carry out monitoring

40 operations on a small, medium and large scale (Jordan et al. 2017). The accuracy of 3D information can be significantly increased by the ground control points (GCPs). The GCPs aquisition is a fondamental aspect of the georeferencing of the network of images captured by UAV photogrammetry. In this process a right number of GCPs is required which lead to a greater accuracy of the outcomes (point clouds, 3D grid, orthomosaic or digital surface model (DSM)). The precision of the outcomes is also affected by other features, for example: the focal distance of the camera, the design and altitude of the

45 flight, the orientation of the camera, the picture quality, the processing chain, the category of UAV system (fixed or rotary wings).

In this paperthrough SFM, we present the results and analysis of the surface deformation monitoring of the mud volcano of Santa Barbara (Caltanissetta, central Sicily) (Fig.1). We have applied the statistical analysis of significant changes with 95% (LoD 95%) Level of Detection. In detail, we monitored the volcano, using precision maps and the M3C2-PM (Lague et al.,

50 2013; James et al., 2017b) algorithm to determine the surface variations. The statistical analysis allows to verify i) the uncertainty between the different surveys, ii) the spatial variability of the accuracy in the surveys (James et al., 2017/b), iii) the quality of the georeferencing of the surveys based on the number of GCPs.
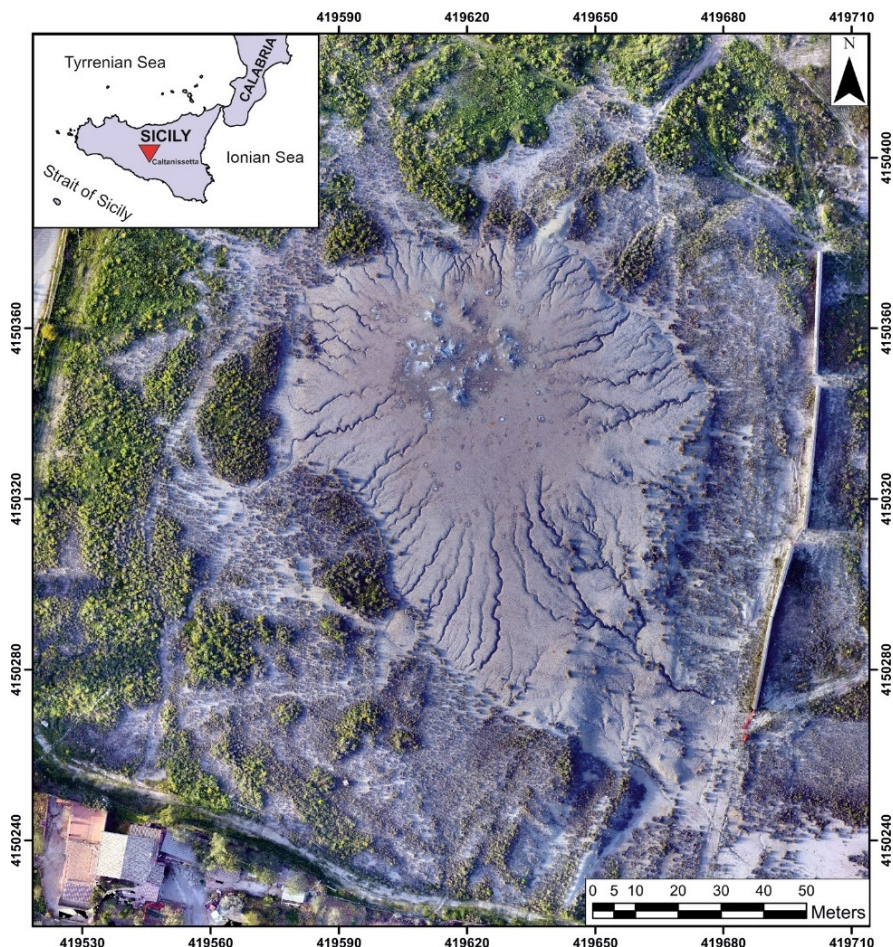
Figure 1: Ortho-photos generated by UAVs in the area of the Santa Barbara mud volcano.

The mud volcano of Santa Barbara is located within the Caltanissetta foredeep basin of the Apennines-Magrebian collisional chain developed since Late Miocene untill the Quaternary, along the border of the converging Eurasia-Nubia plate (Catalano et al., 2008; Dewey et al., 1989; Serpelloni et al., 2007). This structural domain is formed by foreland fold and thrust belt involving the clastic sediments deposited which were gradually contracted and moved during the late Miocene towards the Pleistocene (e.g. Monaco and Tortorici, 1996; Lickorish et al., 1999, and references therein).

According to Madonia et al., (2011) mud volcanoes are most of the time in stasis, but they are a preferential way for rising fluids rich in methane and sludge therefore they can be considered a risk to urbanized areas or sites with an economy dedicated to natural attractions.

On the mud volcanoes, geomorphic/structural features have been observed from one year to shortly before the paroxysmal event (Antonelli et al., 2017; Madonia et al., 2011). Also, the area of the Santa Barbara volcano was affected in 2008 by

paroxysmal mud eruption which was preceded by deformation features (Fig. 2). More hover the surface of the mud volcanic cone is incised by a drainage system (Fig.1) characterised by hydrographic basins with elongated dendritic geometry arranged to a centrifugal development from the areas of the summit craters towards the lower slopes of the volcano complex.

70   The higher order of the thalwegs present deep recessed meanders (landscape rejuvenation process). This morphometric structure is typical of uplifting areas and therefore relative decrease of the base level. This morphometric evidence suggests uplift processes of the canopy volcano area that lies above a stagnation chamber that has been carried out for this research project through geophysical investigation (personal communication, 2019). The stagnation chamber has a "sills-like" geometry and develops at a depth of about 30 meters for a radius of about 50 and a thickness of about 30 meters. This

75   morphostructural configuration supported by geophysical data configures the active geological structure as a high potential geological hazard.
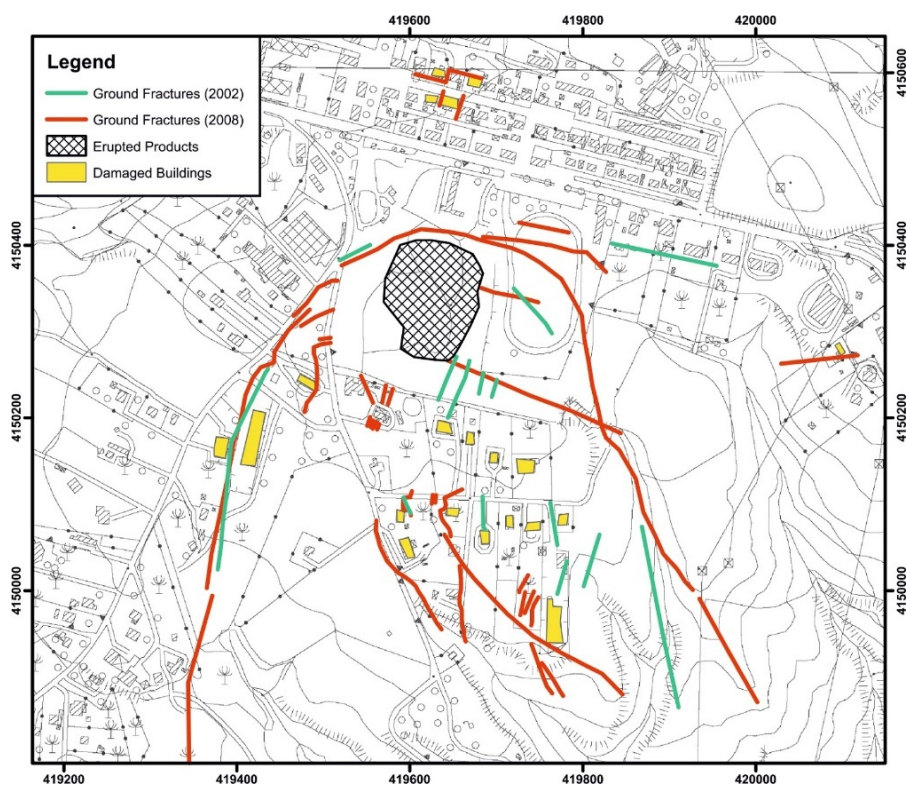
Figure 2: Cartographic extract with the location of the major fractures (in red) found on the ground and the damaged structures
80   **(in yellow) related to the paroxysmal event of 2008. In green fractures found in 2002.**

On the surface outcrops deformation structures (fractures and shear lineaments) with geometry extending outside areas of the volcano, (Madonia et al., 2011; Bonini et al. 2012; INGV, 2008a; Regione Siciliana, 2008) highlighting what high intensity

of stress and strain the volcano can generate (Fig.2). Such structures have been detected in the past and we still believe they

85   are active, and whose development has often been a precursor of paroxysmal events such as the one that occurred in the 11th August 2008 event (INGV, 2008a; Regione Siciliana, 2008).

2 Methods

2.1 Local Network

90

In order to monitoring active deformation in the mud volcano area, a restricted GNSS network was created according to the criteria described by De Guidi et al (2017), in particular: i) ensuring the basic requirement of spatial and temporal stability ii) absence of possible gravitational instabilities in both static and dynamic conditions at sites; iii) moreover a panoramic and elevated position of Theodolite Total Station.

95   According to these criteria a two GNSS benchmarks were created: CTN0 and CTN1, located on the roof of a building on the northern sector of the studied area (Fig.3).
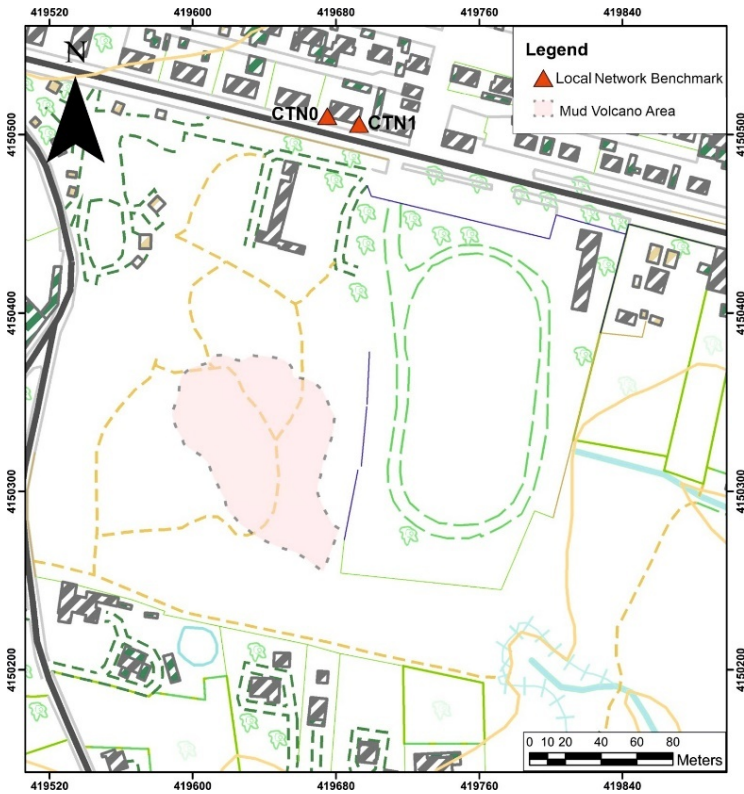
Figure 3: Chorography of the eastern periphery of the inhabited area of Caltanissetta (Santa Barbara Village).

100

The benchmarks were surveyed using double frequency (L1/L2) receivers (TOPCON Hiper V and HiPer SR) in static mode. Once the stability of the benchmarks has been assessed, we surveyed CTN0 and CTN1 5 and 2 times respectively.

Post processing of GNSS data was carried out by AUSPOS Online service (Geoscience Australia, 2011; Jia, M et al., 2014).

To process the CTN0 data of 28/02/2018 survey, AUSPOS used 15 IGS stations to computed the baselines: ANKR, BOR1, 105 BRUX, BUCU, GANP, GRAS, GRAZ, LROC, MAT1, MEDI, SOFI, TLSE, VILL, YEBE and ZIM2 with an average of ambiguity resolution of 90.0%, position uncertainty (95% C.L.) are respectively of 0.005 m, 0.005 m, 0.016 for East, North and Ellipsoidal height.

To process the CTN1 data of 26/11/2018 survey, AUSPOS used 15 IGS stations to computed the baselines: ANKR, BOR1, BRUX, BUCU, GANP, GRAS, GRAZ, LROC, MAT1, MEDI, SOFI, TLSE, VILL, YEBE and ZIM2 with an average of 110 ambiguity resolution of 84.5%, position uncertainty (95% C.L.) are respectively of 0.007 m, 0.007 m, 0.024 for East, North and Ellipsoidal height.

Finally, the best ITRF2014-UTM coordinates (with the less error) have been assigned to the TST base local station and to the orientation point.

115

2.2 Ground Control Points (GCPs)

During the monitoring sessions there has been ongoing research on the best Ground Control Points (GCPs) methods of acquisition. This was aimed at a more detailed indication of the 3D deformation process of the volcanic cap and a vertical and horizontal geometrical resolution of centimetre/subcentimetric order of magnitude.

120 Initially (2016-2018) we used only GNSS receivers in different configurations (Real Time Kinematics, Static Ultra Rapid), while the GPC were made of 50cm x 50cm alveolar polypropylene square targets. With these configurations (Tab. 2), errors ranging from 10-1 ÷ 10-2 m were recorded. With Static Ultra Rapid mode the total error was about ≈18 cm whereas with the RTK configuration we recorded a reduction of the error up to ≈ 4 cm (Brighenti et al, 2018 Poster).

From 2018 the use of the TopCon DS-103 Total Station Theodolite DS-103 (TST) was introduced, obtaining lower values
125 on the GCP error than those detected with the GNSS technique (Tab.1). With this measurement technique the error has been reduced to ≈ 3 cm.

The statistical analysis is generated by the SfM software (Photscan v. 1.4) and using 6 GCP (Fig.4) for georeferencing the first 3 campaigns, which were not used in this work.

Since 2019 only TST has been used for the GCP survey and according to Tahar et al. (2013) the number of GCPs has been
130 increased (Tab.1) reducing the error to ≈ 1.4 cm and in the last campaign ≈ 0.7 cm. In particular, the increase of GCPs up to a limit number, as well as their uniform distribution over the measurement area, guarantees a greater control of the geometry of the model obtained from the SfM (Fig.4).

DATE	METHOD OF SURVEY	GCPs NUMBER	X ERROR (CM)	Y ERROR (CM)	Z ERROR (CM)	TOT ERROR (CM)	IMG (PIX)
2018/02/28	Static Ultra Rapid	6	12.06	8.85	10.02	18.01	0.587
2018/04/16	Real Time Kinematic	6	2.18	1.79	3.34	4.29	0.326
2018/04/16	TST	6	2.04	1.39	1.68	2.99	0.325

2019/07/29	TST	29	0.78	0.95	0.72	1.43	0.244
2019/09/13	TST	30	0.79	0.84	0.86	1.45	0.316
2019/10/14	TST	31	0.78	0.66	0.78	1.29	0.311
2020/01/13	TST	31	0.95	0.82	0.77	1.48	0.237
2020/06/15	TST	26	0.43	0.39	0.45	0.73	0.249

Table 1: Average RMSE of GCPs obtained for each survey and for each technique used to determinate the GCPs coordinates: X (Easting), Y (Northing), Z (Altitude) and the average total 3D error. The image residual (IMG, on the table) is shown.
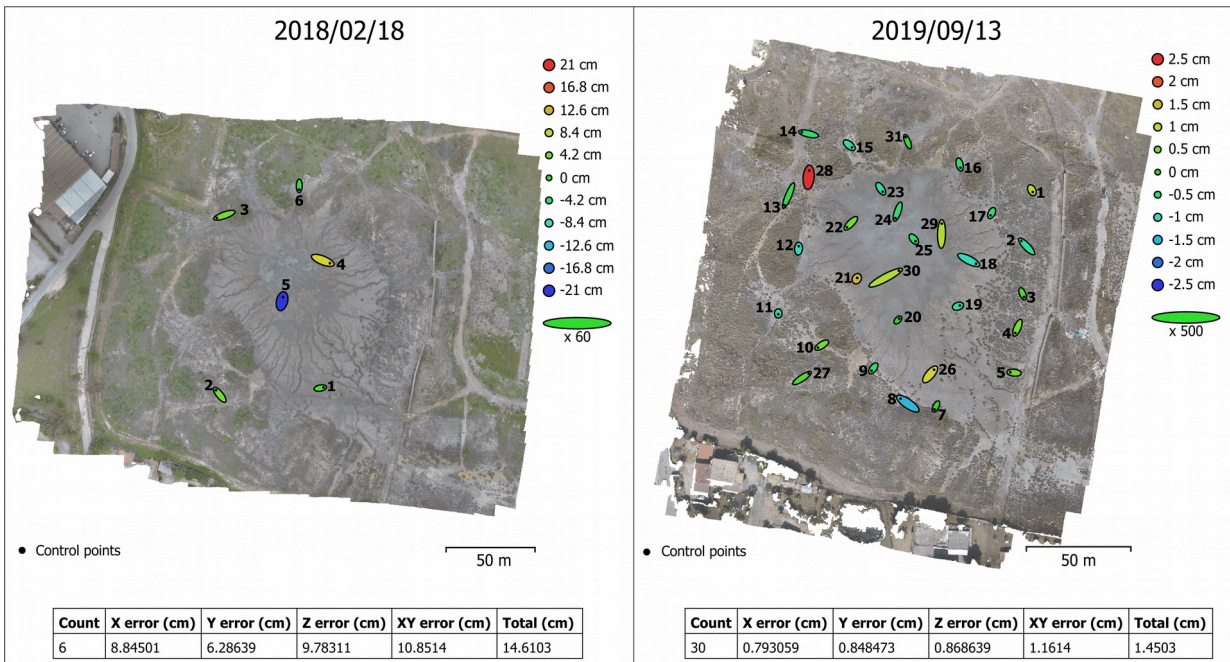
Figure 4: GCPs locations and error estimates. Z error is represented by ellipse colour. X, Y errors are represented by ellipse shape. Estimated GCP locations are marked with a dot. Note the different scale of the error ellipse, in the left image of 2018/02/18 the ellipse is enlarged x60, in the right image of 2019/09/13 it is enlarged x500.

In the 2019 and 2020's campaigns to measure the GCPs we have used just the TST, placed on the CTN0 point in the local grid, (Fig.3) which coincide with the roof of the nearby private houses in the northern part (Fig. 5 A). A classic celerimetric survey was carried out.

The measurements of the GCPs were carried out with a surveying ranging rod equipped with a reflecting prism (offset of -30 mm) assisted by a tripod with a bubble level (Fig. 5 B), to ensure the verticality and stability of the measurement.

Figure 5: A) TST DS 103 placed on the fixed metal base in coincidence with point CTN0. B) Surveying ranging rod on the mud
150 **volcano during the survey phase.**

Based on the CTN0 point and directing on the CTN1 point, we assumed an instrumental error of 5 mm (Photoscan accuracy). This value has been assumed having in mind the uncertainty of the CTN0 and CTN1 points coordinates, obtained through GNSS measurements, without considering the uncertainty derived from the TST.

155 To validate GCPs data we have done a stronger analysis (compared with the SfM software data) using the python script "Monte_Carlo_BA.py", with a statistical iterative approach (Monte Carlo approach) (James et al. 2017/a). This script modifies the GCPs percentage that is used as checkpoint and applies some random variations (James et al. 2017/a). To be more precise values ranging from 10% up to 80% of GCPs have been set.

160
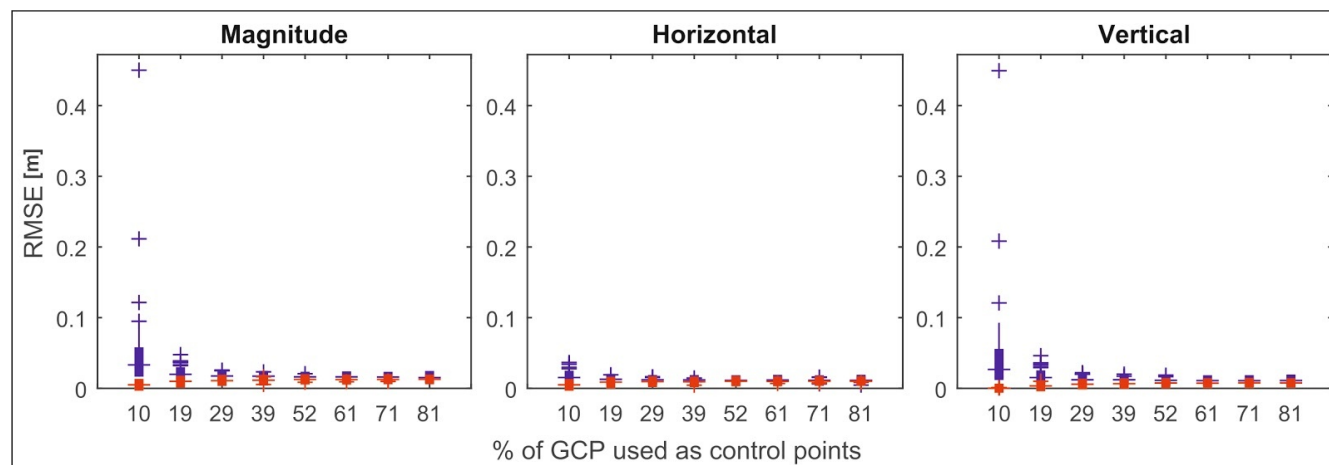
Figure 6: The boxes represent the distribution of the RMSE of GCPs (2019/09/13 survey) on the three components: Magnitude (Total), Horizontal and Vertical according to the % of the GCP used as control points. RMSE is calculated on 50 self-calibrating bundle adjustments for each % of GCPs used as control points. The GCPs are randomly selected for each self-calibrating bundle adjustments. The central bars indicate the median RMSE values, which are included in the boxes that extend from 25° to 75°

165 **percentile and the outliers are indicated by the + symbols.**

Data show that using between the 40% and 60% GCPs, the RMSE value of GCPs vs Checkpoint has a slight minimal variation. Thus, the optimal minimum number of GPCs can be said to be between 12 and 18 GCPs. Exceeded the threshold of 60% up to 80% there are no significant improvements (Fig.6). The trend has been recorded in every campaign.

170 These data give us important indications for the design of future surveys, improving efficiency and therefore optimizing the time dedicated to the acquisition of GCPs.

2.3 Photo Acquisition

We have performed five measurement campaigns in approximately one year. The same flight plan was used for all five of

175 them. The AOI (area of interest) was captured by a DJI Phantom 4 Standard, a cheap UAV, fly altitude33 m above ground. The feature of the UAV's digital camera is a 6.17 mm by 4.55 mm image sensor, capable of shooting images with a resolution of 12 MP (4000 × 3000 pixels) with a mechanical shutter. Each flight planning was carried out with the Pix4D Mapper software, adopting a frontal and side overlapping of 80% and 70% respectively. The camera was oriented in a 90-degree angle. The flight was carried out in a single grid. About 280 images were acquired with about 1.1 cm GSD.

2.4 Data Processing SfM

180

The photogrammetric processing was performed using Agisoft PhotoScan v. 1.4, a commercial software already used in many articles on SfM techniques. The photogrammetric processing is based on the workflow formulated by the USGS (2017) with the values of Tie Point Accuracy and Marker Accuracy recommended in James et al. (2017) (Fig.7).

Step 1

Photo Setup, Alignment, Initial Adjustament

Add Photos
↓
Set Coordinate/Projection
↓
Camera Calibration
↓
Align Photos
↓
Initial Bundle Adjustament
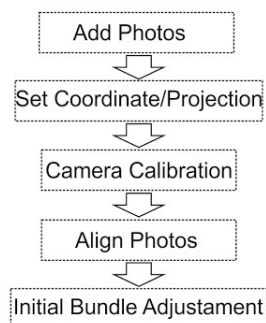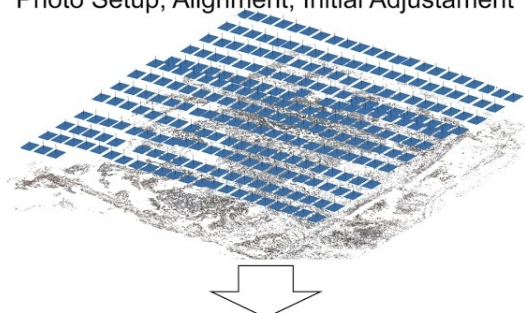
Step 2

Error Reduction & Bundle Adjustament

Recustruction Uncertain ← Repeat Until Set Level 10
Bundle Adjustament
↓
Projection Accuracy ← Repeat Until Set Level 2-3
Bundle Adjustament
↓
Tighten Tie Point Accuracy Value
Bundle Adjustament
↓
Add Control Points (Markers)
Bundle Adjustament
↓
Reprojection Error ← Repeat Until Set Level 0.3
Bundle Adjustament
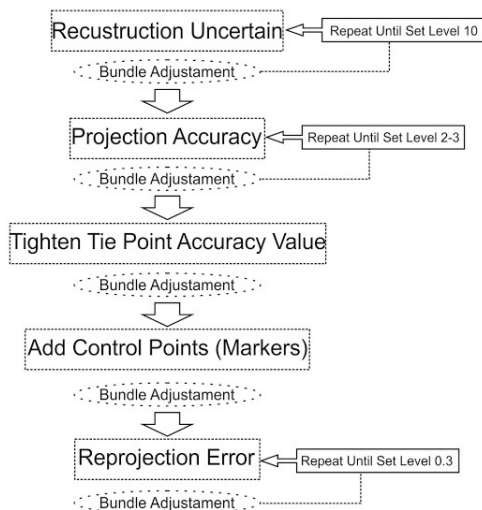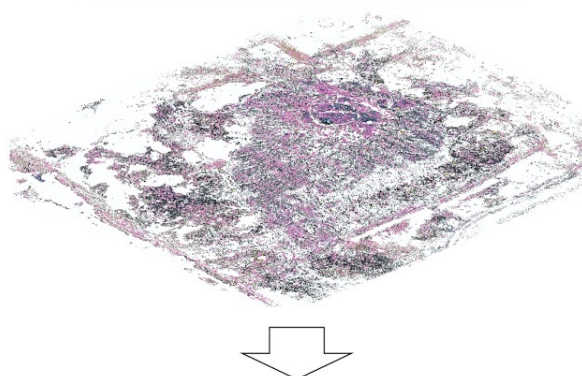
Step 3

Build Dense Point Cloud,Mesh,Texuture,
DEM, Orthomosaic

Build Dense Cloud
↓
Build DEM
Build Orthomosaic
Build Mesh
Build Texture
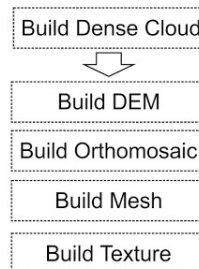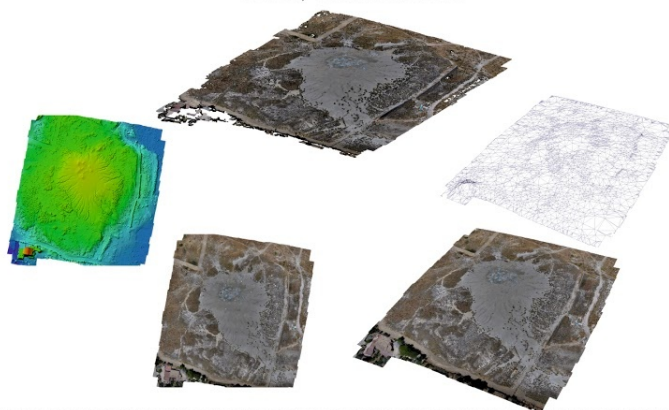
185 **Figure 7: Simplified block diagram of the photogrammetric processing chain.**

While the procedure followed was conventional, we can underline how in the workflow particular attention was put on the cleaning of the sparse point cloud using the "Gradual Selection" function, in the "Reconstruction Uncertain" and "Projection Accuracy" values, and then on the "Reprojection Error" after having georeferenced the model (coupling of the GCPs).

190   The first value, "Reconstruction Uncertain", is used to improve the geometric reconstruction of the cloud point.

The second one, the "Projection Accuracy", is aimed at improving pixel mismatches in images.

After these operations, the GCPs can be hooked to the cloud point.

Once the georeferencing procedure has been performed, we have to perform the Gradual Selection function, adjusting the "Reprojection Error" values to reduce the Residual Pixel Errors.

195   Furthermore, appropriate pixel values of tie point accuracy and marker accuracy are set, following suggestions presented in the paper written by Jemes, et al. (2017 / b).

Remaining in PhotoScan, we applied the "presciosion_estimate.py" script (Jemes, et al. 2017 / b). The script operates, through an interactive Monte Carlo approach, to estimate the accuracy of topographic surveys based on SfM, including photogrammetric and georeferencing parameters, which are then used to provide spatially variable confidence limits for the

200   detection of surface variations.

The precision estimates are calculated through multiple "bundle adjustments" ("Optimize Camera Alignment" in PhotoScan) with different pseudo-random offsets (in this case 4000 were used) (Fig. 8), applied to the image observations and measurements of check for each of them. Offsets are derived from normal distributions with standard deviations representative of the appropriate measurement accuracy within the survey (James et al. 2017 / b).

205
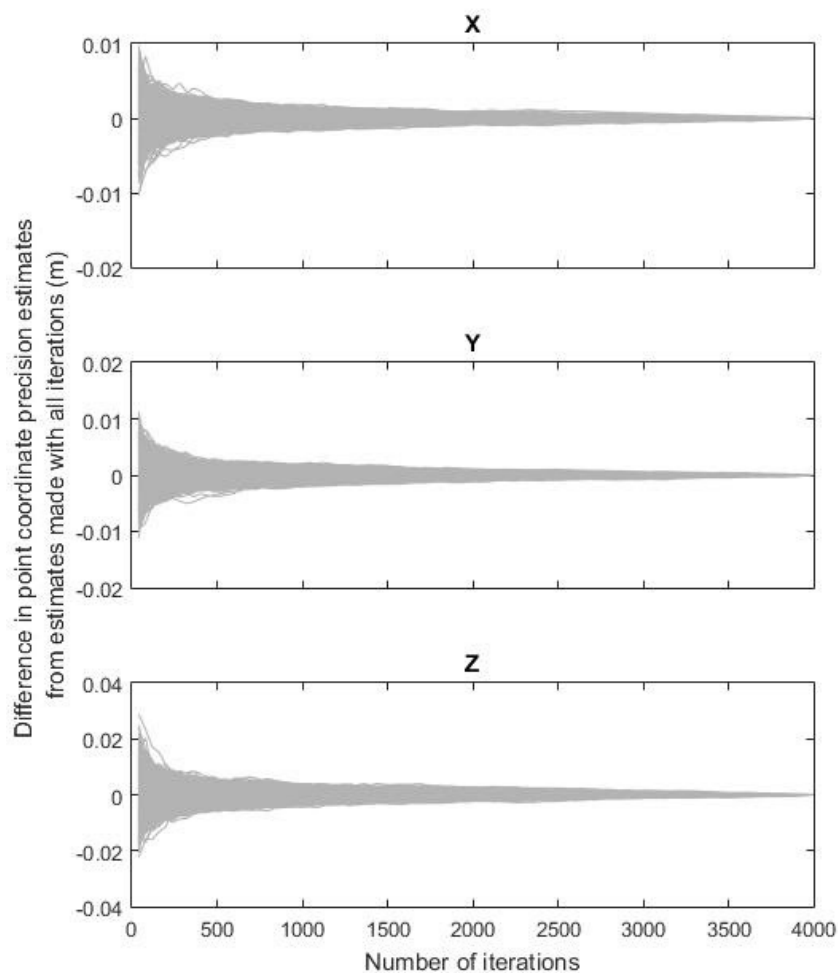
Figure 8: Example of the iterative approach in the 2020/07/29 survey. Estimates of uncertainties on X, Y and Z improve as iterations increase.

210   Secondly, the Sfm-Georef software (James and Robson, 2012) reads the output given by the Monte Carlo python script, setting to each point of the sparse cloud precision different values on the three spatial components. The results of the script, read by Sfm-Georef, are estimates of the error of the individual points of the sparse cloud point in the three different spatial dimensions. The 3D topographic change is usually detected from scattered cloud points that have been cleaned to exclude the vegetation that interferes with the measurements as much as possible. Next step is to link those points to the precision

215   estimates of the sparse cloud; this has been done in CloudCompare.

Through CloudCompare the sparse cloud is interpolated (with the relative precision values on the three-dimensional components) with the dense cloud point. In this phase we decide which interpolation technique is the more suitable, in our case the best is "nearest neighbors" that consider the three closest points to the sparse cloud, using the median value (better outliner mitigation) to give the scalar values to the dense cloud points. This methodology has been chosen having in mind 220 the heterogeneous distribution of the points in the sparse cloud, avoiding holes and thus null values.

Comparisons between the measurements were performed by means of the M3C2-PM method (James et al., 2017B; Lague et al., 2013) that identifies a statistically significant change where the topographical differences exceed a value of spatially variable uncertainty. The M3C2-PM variant (James et al., 2017/b) uses estimates of precision of the coordinates of points that we have previously calculated. Therefore, the M3C2-PM algorithm can be used for point clouds derived from SfM.

225 The main outputs of this processing are scalar values applied to the cloud:

- significant change (Fig.9 A);
- M3C2 distance (Fig.9 B);
- distance uncertainty (Fig.9 C).

The first output highlights where the uncertainty values in both point clouds have been exceeded, representing a confidence 230 interval constrained by values of $LoD_{95\%}$ (Level Of Detection $_{95\%}$) which are spatially variable, this is applicable in any type of terrain, providing a reliable 3-D analysis of topographical change.

The second output shows the calculated distances between the two clouds (M3C2 distance using the significant change as a reference for the scale).

235
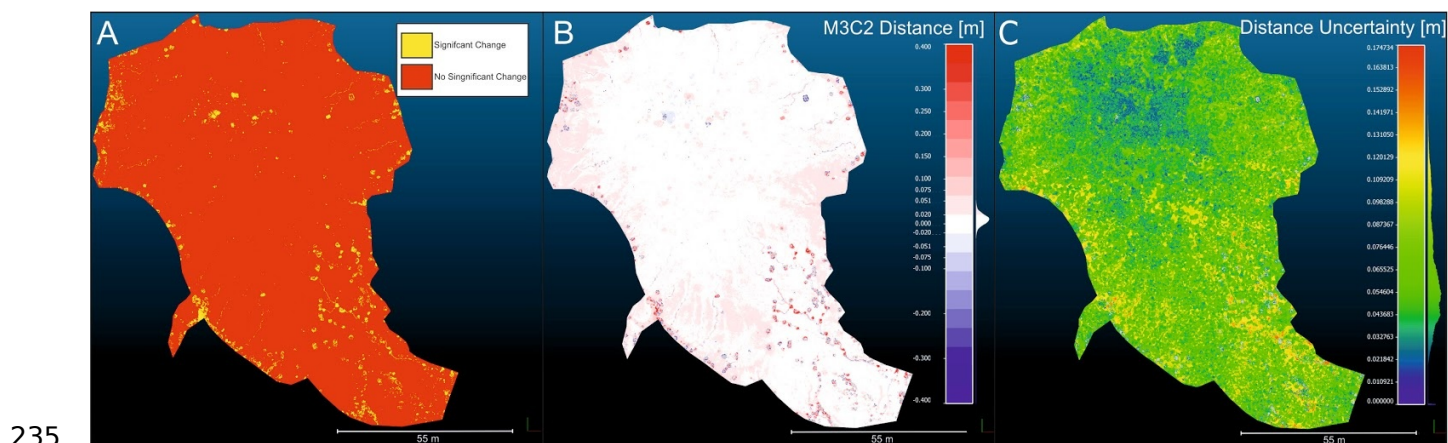
Figure 9: Point clouds resulting from M3C2-PM processing, comparison between 2019/07/29 and 2020/06/15; A) significant changes between the two clouds with LOD95; B) distances between the two point clouds; C) uncertainty of the distance between two clouds.

240 The third output shows the uncertainty values of the distances with spatial variation between the two clouds, which gives the uncertainty value that must be passed to have a significant variation. During the monitoring period, in addition to natural changes, we recorded anthropogenic changes, due to unauthorized access to the study area, with the displacement of objects of various kinds (garbage) in the area. These changes have a decimetric order of magnitude and are easily recorded by the technique used (Fig. 10).

245
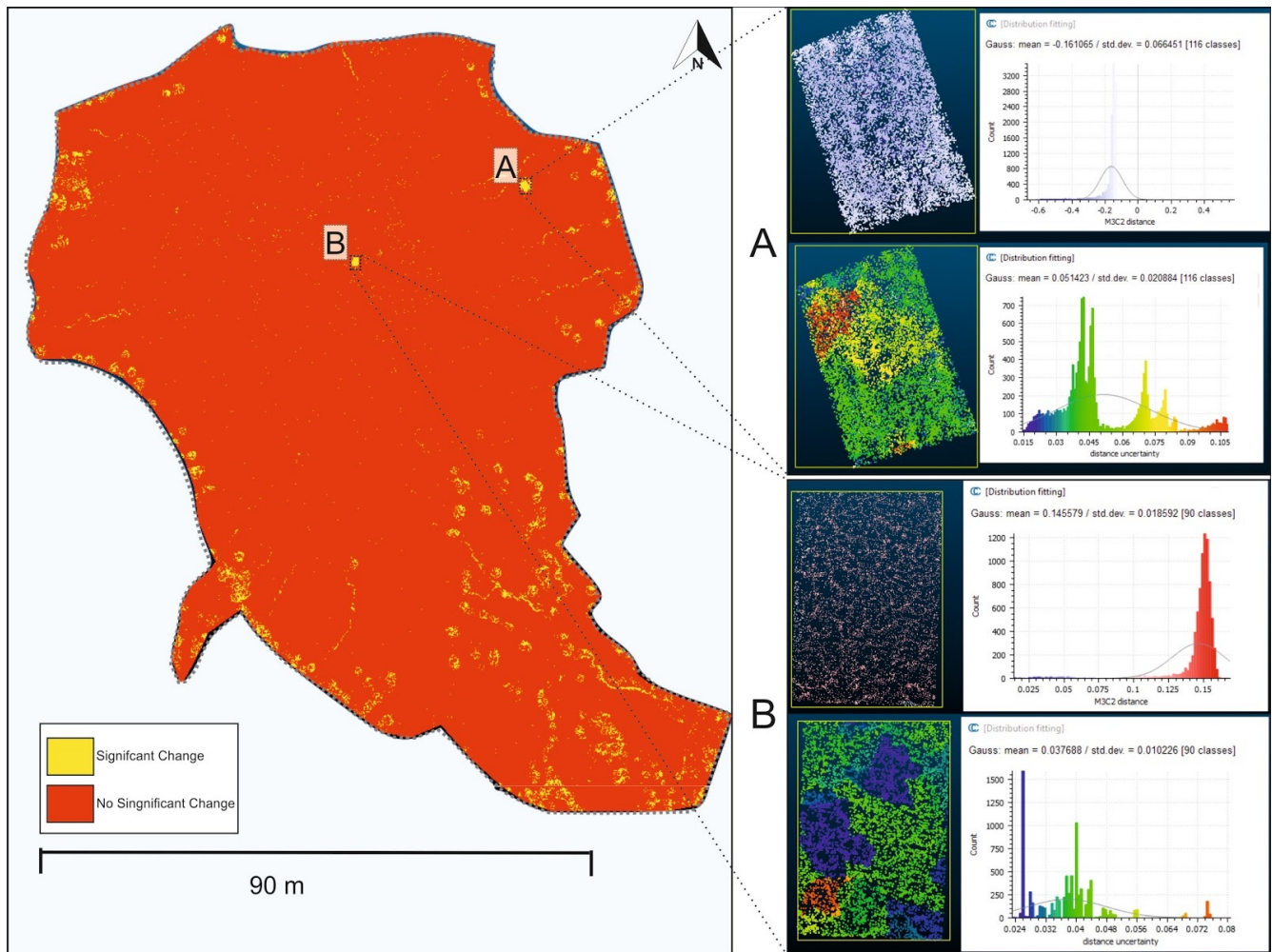
Figure 10: Enlargement of the comparison between the point clouds of the 2019/09/13 and 2019/10/14 campaigns with active Significant Change. We show two significant changes (A and B), which highlight an anthropic action, i.e. the movement of a

250 **wooden platform about 15cm high. A) a lowering of an average height of 16 cm is detected (on the right plot of the Gaussian distribution of the values representing the distances M3C2-PM, mean and standard deviation are indicated); in the lower graph the Distance Uncertain varies spatially and has an average value of about 5 cm (on the right plot of the Gaussian distribution of the values representing the uncertainty of the distance mean and standard deviation are indicated). B) it registers an increase of altitude of 14 cm (on the right plot of the Gaussian distribution of the values representing the distances M3C2-PM, mean and standard deviation are indicated) and the distance uncertain has an average value of about 3 cm (on the right plot of the Gaussian**
255 **distribution of the values representing the uncertainty of the distance mean and standard deviation are indicated).**

In the survey carried out in 2020/06/15, we used calibers to test the accuracy of the measurements and further test the validity of the method. Five numbered calibers, with steps of increasing height of about 2 cm, were positioned on the mud dome (Fig. 11). The heights are approx.2, 4, 6, 8, 10 cm. (Fig.11).

260

Figure 11: Rectangular calibres made to observe the sensitivity of the technique used in the comparison of point clouds.

These were used to have an instrumental sensitivity scale of the measures of figure 12. The first and lowest one (≈2 cm) was
265 easily detected.
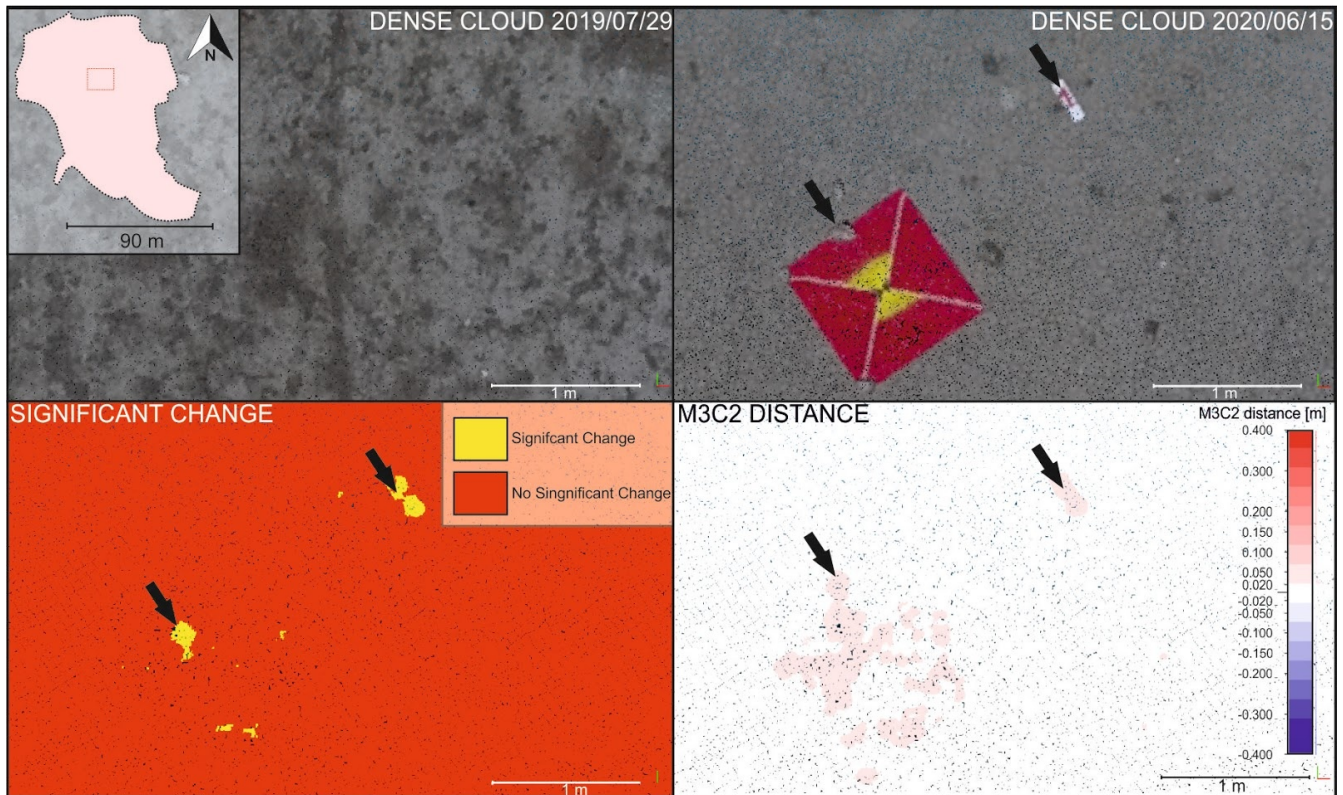
Figure 12: On the upper part of the figure the point clouds of the two surveys carried out on 2019/07/29 (left) and 2020/06/15 (right) are shown. In the lower part the clouds with the significant change (left) and the M3C2 distance (right). The arrows
270 **indicate the significant changes in the two surveys compared. The calculated changes between the two clouds estimate an altitude increase of ≈6.3 cm for the fragment of rock used to maintain the target in position and an increase in height of ≈2.5 cm for the calibre, ≈2 cm thick.**

3 Discussion

275 The results obtained from the photogrammetric study supported by geodetic topographic survey techniques, they have a very low uncertainty compared to the working scale with an average uncertainty of about 6.4 cm, with a minimum of about 2 cm and a maximum of about 12 cm, relative to an area of 42700 m²(Fig.13/A). The uncertainty, analysing only the area of the central shell, has an average value of about 3.9 cm, with a minimum of about 2 cm and maximum of 10 cm, for an extension of 360 m² (Fig.13/B).

280
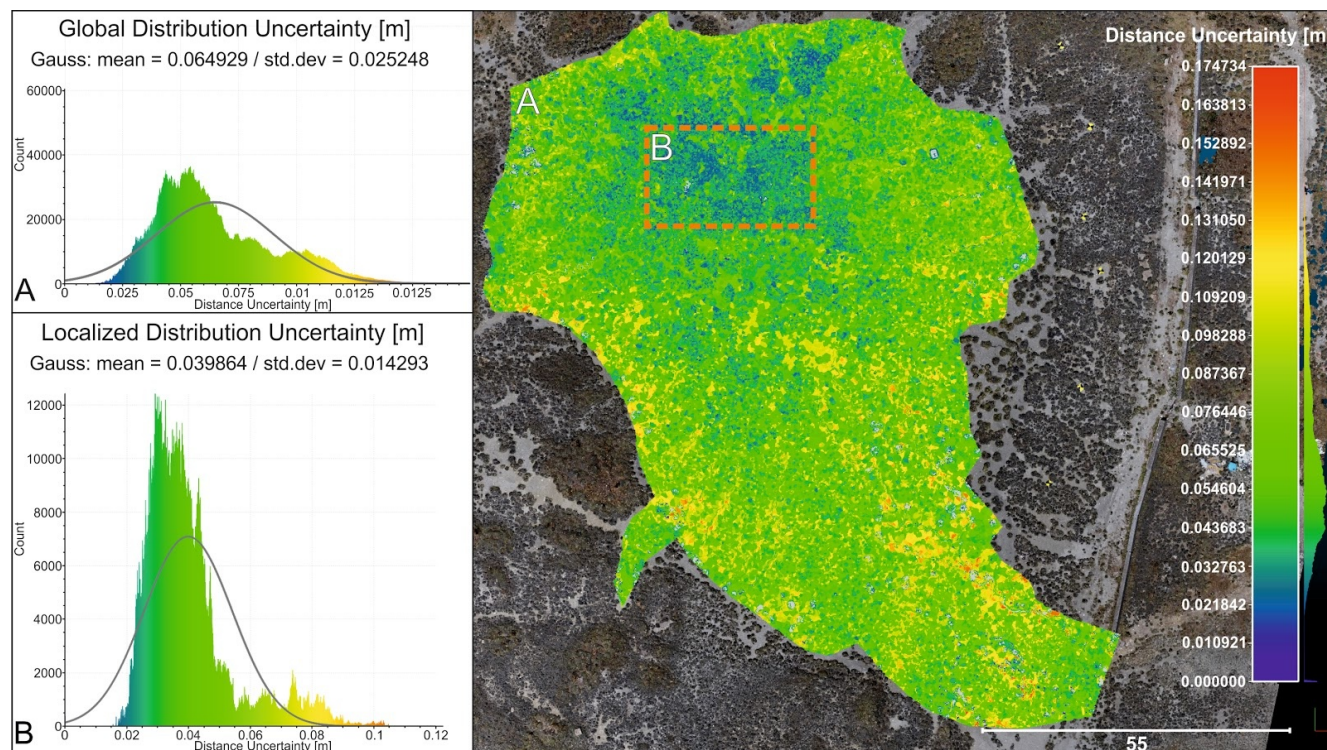
Figure 13: Cloud of points with uncertainty distance values between 2019/07/29 and 2020/06/15 (right). On the left, (A) the Gaussian distribution of the distance uncertainty over the whole survey is shown, the mean is about ≈6.4 cm and the standard deviation is about ≈2.5 cm.(B) the Gaussian distribution of the distance uncertainty of the central emission area is shown, the mean is about ≈3.9 cm and the standard deviation is about ≈1.4 cm.

The analysis of point clouds calculated for each of the five measurement campaigns, has statistically valid results at the 95% confidence with spatial variations. To observe the change, we selected the two most temporally distant peaks (about 1 year). we have set a scale with null values from -2 cm to 2 cm (Fig. 14), although in this case not statistically valid, but instrumentally verified with the use of gauges. Data are still useful to detect anomalous deformations as alert elements (Fig.11). This result is important from the point of view of monitoring and controlling the deformation of the volcanic shell, since severe cases of deformations, driven by changes in pressure and volume of fluid, may occur in relation to the major eruptions. The pre-eruptive deformation consists of a marked uplift and occasional small subsidence which are probably related to the redistribution of the subsoil of the pressurized fluids (Antonelli et al. 2014). In literature, soil lifting can occur up to a year before the eruption (Antonelli et al. 2014).
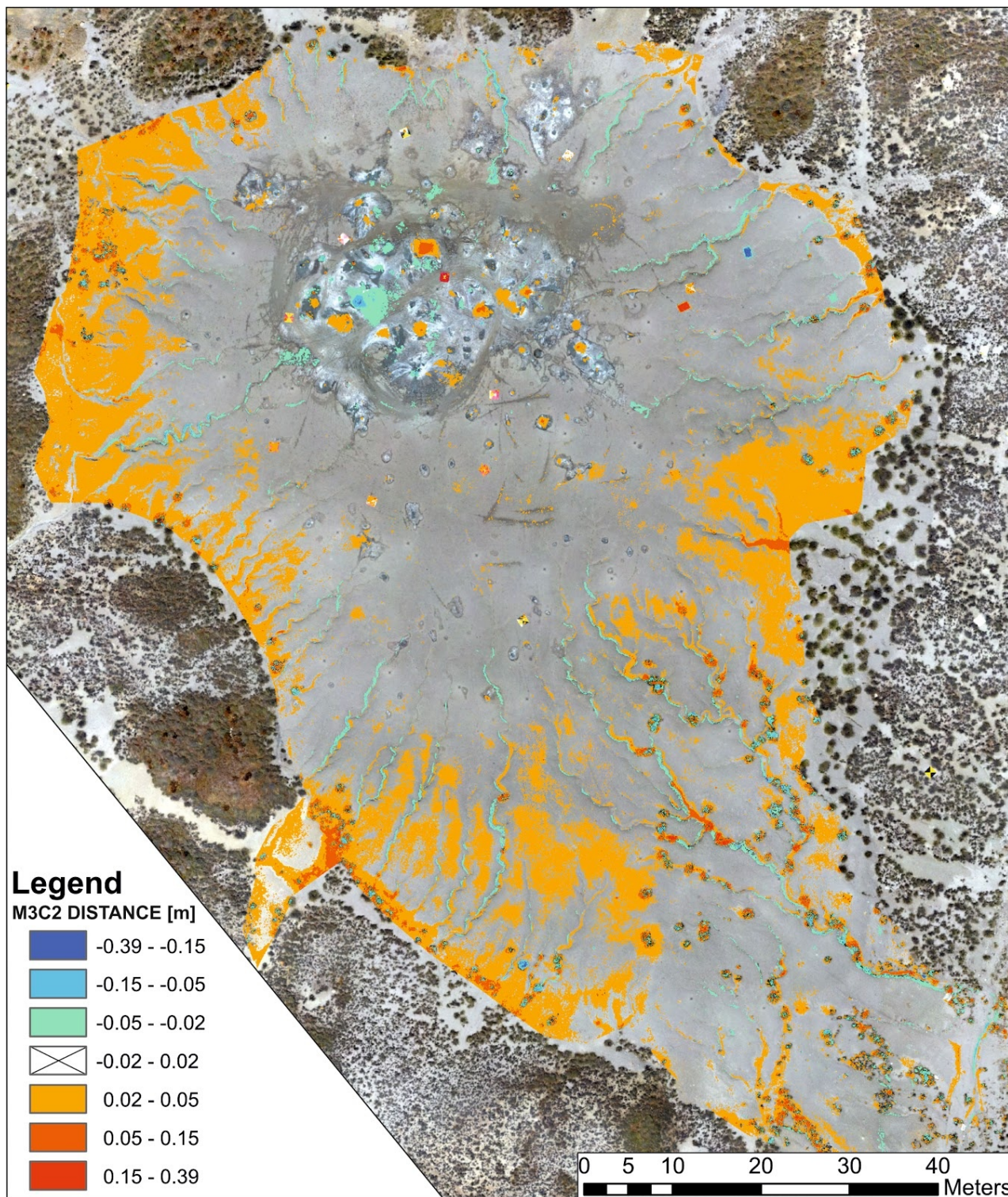
Figure 14: Orthophoto with M3C2 Distance, the distance scale has been adjusted to exclude values from ± 2 cm.

300   In order to assess the deformation and the local morpho-structural evolution rates two temporal series have been developed in two areas C1 (collapse zone) and C2 (lifting zone) (Fig.15 and Fig.16). The zones were chosen by the significant change ratio, using the average value of the distances of the points calculated by M3C2-PM, for an extension of 1 m² and 0.84 m² for C1 and C2 respectively.

As master was chosen the campaign of 07.19.29 (T0) and subsequent as a slave (Table 2).

305

T_0	2019/07/29
T_1	2019/09/13
T_2	2019/10/14
T_3	2020/01/13
T_4	2020/06/15

Table 2: Used time series.
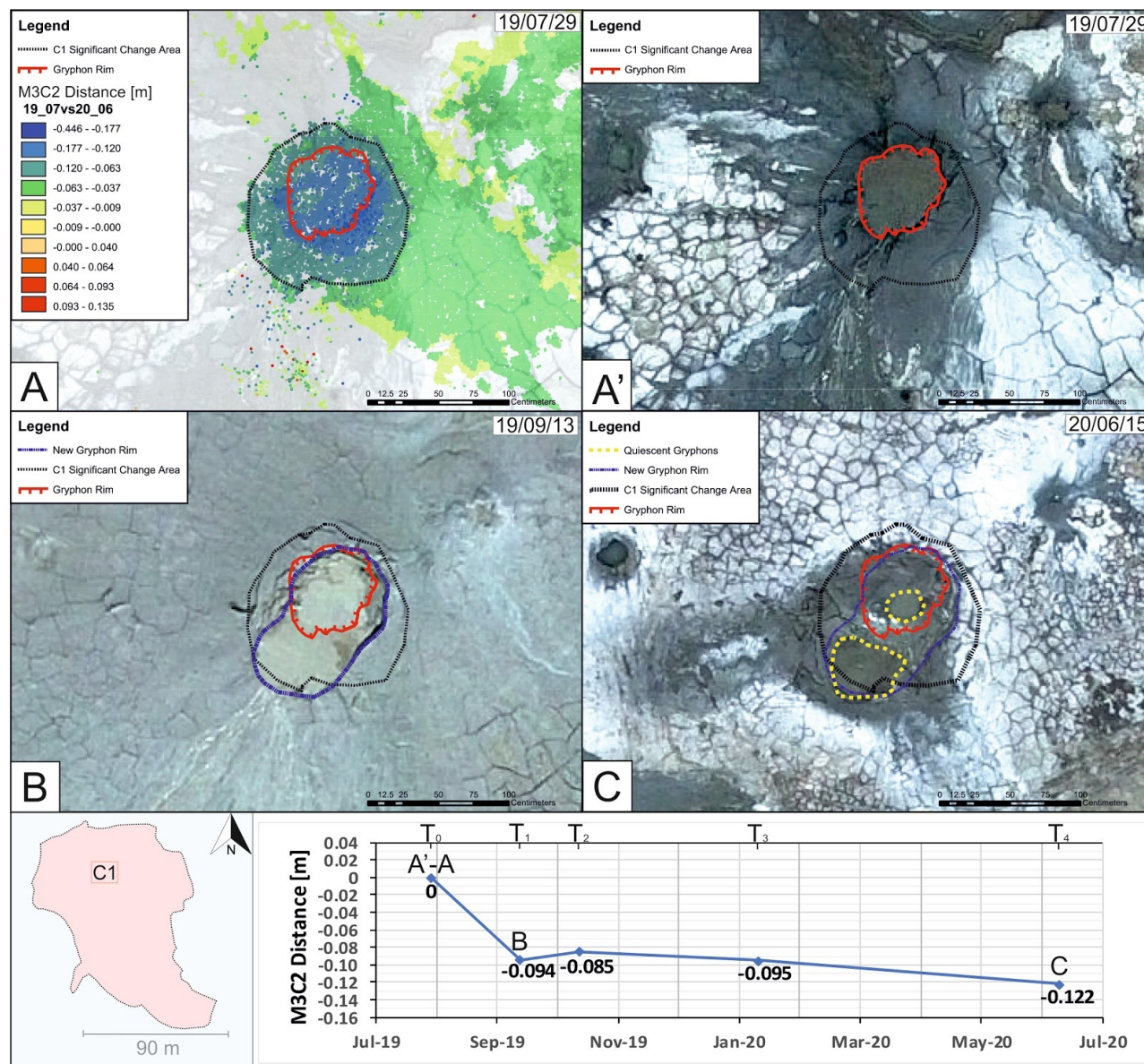
Figure 15: A) Orthophoto of 2019/07/29 with M3C2 Distance (2019/07/29 vs 2020/06/15), highlighted area C1 with significant changes used to create the time series. A') Orthophoto of 2019/07/29 with the gryphon border in red. B) Orthophoto of 19/09/13, enlargement of the gryphon border in blue. C) Orthophotos of 2020/06/15, gryphon during the quiescence phase and the split of the channel in yellow. Below the time series with a decreasing trend is shown.

At the end of the five survey campaigns (2019/07/29 - 2020/06/15) (Fig. 14) we can observe that the total surface of the volcanic cone can be considered not affected by deformations. Only morphological changes in the volcanic structures can be

underlined, such as small eruptive cones, griffins, sauces and mud pools. In figure 15 the rapid subsidence (about 10 cm / 60 days) of a griffon vulture is represented by the southwest migration of the mud pool edge. In figure 16, the rapid uplift (about 4 cm / 60 d) of a blind griffin is represented by the development of radial fractures on the cone surface. Close to the growing

320   cone, another indication of this deformation is the deviation of a mudslide flowing in the N-S direction towards the southern sector of the analysed area. Finally, the sudden appearance of the cone is well highlighted in the photo of the last survey of the campaign (Fig. 16).
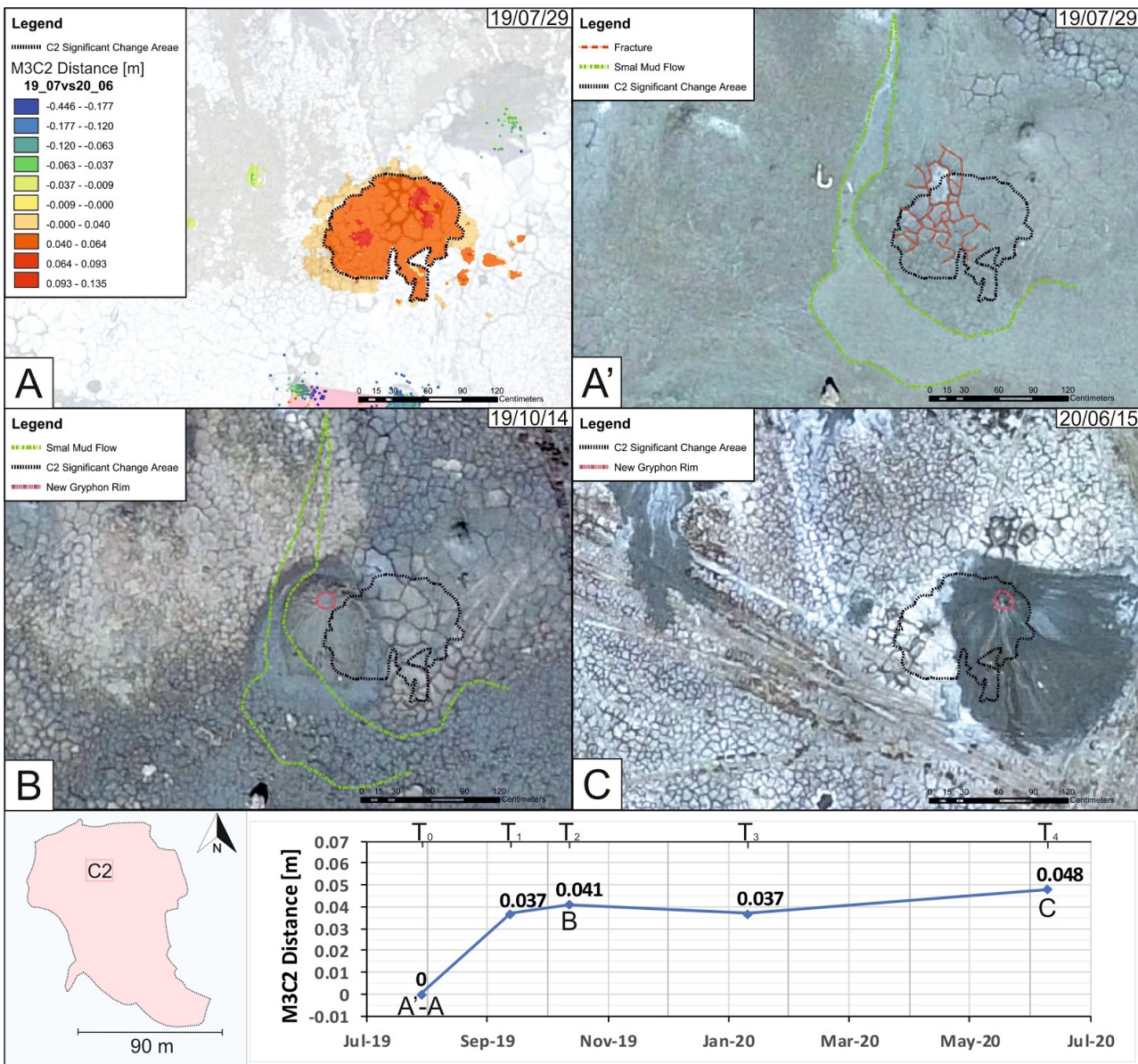
Figure 16: A) Orthophoto of 2019/07/29 with M3C2 Distance (2019/07/29 VS 2020/06/15), the area C2 with significant changes
325 **used to create the time series is delimited with a dashed line. A') Orthophoto of 2019/07/29, the margin of the deflected flow, in**
green, and the radial fractures, in red. B) Orthophoto of 19/10/14, formation of a new emission cone in red and the previous flow
in green. C) Orthophoto of 2020/06/15, formation of a new emission cone, in red. Below the time series with upward trend is
shown.

330 **4 Conclusion**

In recent decades, high-resolution digital photographs have been used, thanks to the use of software based on SfM, to
generate high-quality topographic information. In geosciences many studies have been dedicated to morphological processes
(Casella et al., 2014; Castillo et al., 2012; Dietrich, 2016; Eltner et al., 2015; Gomez-Gutierrez et al., 2014; James and
Robson, 2012; James and Robson, 2014b, James and Varley, 2012; Javernick et al., 2016; Lucieer et al., 2014; Ryan et al.,
335 2015; Smith et al., 2016; Westoby et al., 2015; Woodget et al., 2015). Applications include runoff laboratory trials (Morgan
et al., 2017), applied geology (Niethammer et al., 2012; Russell, 2016), geomorphology (Bakker and Lane, 2016; Balaguer-
Puig et al., 2017; Dietrich, 2015; Dietrich, 2016 a/b; Heindel et al., 2018; Javernick et al., 2014; Marteau et al., 2016; Mercer
and Westbrook, 2016; Pearson et al., 2017; Prosdocimi et al., 2017; Seitz et al., 2018; Smith and Vericat, 2015; Snapir et al.,
2014; Vinci et al., 2017), glaciology (Immerzeel et al., 2017; Piermattei et al., 2016), coastal morphology (Casella et al.,
340 2016; Brunier et al., 2016; James and Robson, 2012), volcanology (Bretar et al., 2013; Carr et al., 2018 ;James and Robson,
2012). SfM is commonly used in the cultural heritage field for the 3D reconstruction (Jalandoni et al., 2018; Sapirstein,
2016, 2018; Sapirstein and Murray, 2017).

The versatility of the SFM allows its application in many fields, the use of this technique, in the management of the hazard

(Gomez et al., 2016, Kaab, 2000, Fugazza et al., 2018) is beginning to grow in the scientific community. In the monitoring

345 of potentially dangerous active structures its application is very advantageous not only as a support in the post-disaster event,

but for pre-event monitoring.

According to Kopf (2002), Antonelli et al., (2014), Madonia et al., (2011) and (INGV, 2008a; Regione Siciliana, 2008), the

deformations of the surface shell of mud volcanoes can happen up to a year before the event: the deformations of the surface

shell of mud volcanoes can occur up to a year before the event: doming and developing of structural lineaments with order of

350 magnitude from centimetres to decimetres.

The results obtained allow us to define the criteria for monitoring the study area which are:

- Time interval of the measurement campaigns between 30 and 60 g;
- Quantify the optimal number of GCPs between 12 and 18 according to the development surface of the surveyed
  area (42,700 m^2);
355 - Method for acquisition of GCPs through use of high-precision topographical instrumentation (TST);
- Optimization of the processing of the point cloud, acting on the cleanliness of the point cloud (workflow modified
  USG) and on the "Tie Point Accuracy" and "Marker Accuracy" as studied by James et al. (2017).

The frequencies of the campaigns depend on the status of activity, while the other criteria depend on the object / structure of the monitoring.

360 These criteria allow us to detect events with deformation up to 2 cm, detect anomalous values and as a consequence to improve the monitoring campaigns. In this case more thoroughly monitoring will carried out: i) developing time series localized in key areas, ii) combining different methodologies, eg. monitoring of volcanic tremor (Madonia et al., 2011) and three-dimensional geophysical prospecting (Imposa et al., 2016) to improve the monitoring system of the active geological process.

365 **Acknowledgements**

This paper was carried out with the financial support of the Presidenza del Consiglio dei Ministri (Project Code E98D19000000001, Monitoraggio e Studio dei Processi di Deformazione Superficiale Connessi al Vulcanismo-Sedimentario delle Maccalubbe di Santa Barbara (Caltanisetta) within the DPCM 25 Maggio 2016 - Riqualificazione Urbana e la Sicurezza delle Periferie delle Città Metropolitane, dei Comuni Capoluogo e delle Città di Aosta, Scientific Supervisor: G.

370 De Guidi).

We thank Dr. Silvia Rita Popolo for her valuable support.

Finally, we thank also municipal authority of Caltanisseta for collaboration.

References

Altamimi, Z., Collilieux, X. & Métivier, L.: ITRF2008: an improved solution of the international terrestrial reference frame,
375 J Geod 85, 457–473, https://doi.org/10.1007/s00190-011-0444-4, 2011.

Antonielli, B., Monserrat, O., Bonini, M., Righini, G., Sani F., Luzi, G., Feyzullayev, A. A., Aliyev, C. S.: Pre-eruptive ground deformation of Azerbaijan mud volcanoes detected through satellite radar interferometry (DInSAR), Tectonophysics, Volume 637, Pages 163-177, ISSN 0040-1951, https://doi.org/10.1016/j.tecto.2014.10.005, 2014.

Bakker, M. and Lane, S. N.: Archival photogrammetric analysis of river–floodplain systems using Structure from Motion
380 (SfM) methods, Earth Surf. Proc. Land., 42, 1274–1286, https://doi.org/10.1002/esp.4085X, 2015.

Balaguer-Puig, M., Marqués-Mateu, Á., Lerma, J. L., and Ibáñez-Asensio, S.: Estimation of small-scale soil erosion in laboratory experiments with Structure from Motion photogrammetry, Geomorphology, 295, 285–296, https://doi.org/10.1016/j.geomorph.2017.04.035, 2017.

Bemis, S.P., Micklethwaite, S.,Turner,D., James, M.R., Akciz, S., Thiele, S. T., Ali Bangash, H.: Ground-based and UAV-
385 Based photogrammetry: A multi-scale, high-resolution mapping tool for structural geology and paleoseismology, Journal of Structural Geology, Volume 69, Part A, Pages 163-178, ISSN 0191-8141, https://doi.org/10.1016/j.jsg.2014.10.007, 2014.

Boccardo, P., Chiabrando, F., Dutto, F., Tonolo, F.G., Lingua, A.: UAV deployment exercise for mapping purposes: evaluation of emergency response applications, Sensors: 15:15717–15737, https://doi.org/10.3390/s150715717, 2015.

Bonini, M.: Mud volcanoes: Indicators of stress orientation and tectonic controls, Earth-Sci. Rev., 115, 121–152,
390 doi:10.1016/j.earscirev.2012.09.002, 2012.

Bretar, F., Arab-Sedze, M., Champion, J., Pierrot-Deseilligny, M., Heggy, E., and Jacquemoud, S.: An advanced photogrammetric method to measure surface roughness: Application to volcanic terrains in the Piton de la Fournaise, Reunion Island, Remote Sens. Environ., 135, 1–11, https://doi.org/10.1016/j.rse.2013.03.026, 2013.

Brighenti, F., Carnemolla, F., Messina, D., Lupo, M., De Guidi, G. & Barreca, G.: Geo-referencing techniques of 3d models
395 (SfM): Case study of mud volcano, Village Santa Barbara, Caltanissetta (Sicily), 89° Congresso SGI – SIMP, Geosciences for the environment, natural hazard and cultural heritage, Catania, 12-14 September, 2018.

Brunier, G., Fleury, J., Anthony, E. J., Gardel, A., and Dussouillez, P.: Close-range airborne Structure-from-Motion Photogrammetry for high-resolution beach morphometric surveys: Examples from an embayed rotating beach, Geomorphology, 261, 76–88, https://doi.org/10.1016/j.geomorph.2016.02.025, 2016.

400 Carr, B. B., Clarke, A. B., Arrowsmith, J. R., Vanderkluysen, L., and Dhanu, B. E.: The emplacement of the active lava flow at Sinabung Volcano, Sumatra, Indonesia, documented by structure-from-motion photogrammetry, Journal of Volcanology and Geothermal Research, Volume 382, 2019, Pages 164-172, ISSN 0377-0273, https://doi.org/10.1016/j.jvolgeores.2018.02.004, 2018.

Casella, E., Rovere, A., Pedroncini, A., Mucerino, L., Casella, M., Cusati, L.A., Vacchi M., Ferrari M., Firpo M.: Study of
405 wave runup using numerical models and low-altitude aerial photogrammetry: a tool for coastal management, Estuarine, Coastal and Shelf Science 149: 160–167, DOI:10.1016/j.ecss.2014.08.012, 2014.

Casella, E., Collin, A., Harris, D., Ferse, S., Bejarano, S., Parravicini, V., Hench, J. L., and Rovere, A.: Mapping coral reefs using consumer-grade drones and structure from motion photogrammetry techniques, Coral Reefs, 36, 269–275, https://doi.org/10.1007/s00338-016-1522-0, 2016.

410 Castillo, C., Pérez, R., James, M.R., Quinton, N.J., Taguas, E.V., Gómez, J.A.: Comparing the accuracy of several field methods for measuring gully erosion. Soil Science Society of America Journal 76: 1319–1332, DOI:10.2136/sssaj2011.0390, 2012.

Catalano, S., De Guidi, G., Romagnoli, G., Torrisi, S., Tortorici, G., Tortorici, L.: The migration of plate boundaries in SE Sicily: influence on the large-scale kinematic model of the African promontory in southern Italy, Tectonophysics, 449, pp.
415 41-62, 10.1016/j.tecto.2007.12.003, 2008.

De Guidi, G., Brighent, F., Carnemolla, F., Imposa, S., Marchese, S. A., Palano, M., Scudero,S., Vecchio, A.: The unstable eastern flank of Mt. Etna volcano (Italy): First results of a GNSS-based network at its southeastern edge, Journal of Volcanology and Geothermal Research, ISSN: 0377-0273, Vol: 357, Page: 418-424, https://doi.org/10.1016/j.jvolgeores.2018.04.027, 2018.

420 De Guidi, G., Vecchio, A., Brighenti, F., Caputo, R., Carnemolla, F., Di Pietro, A., Lupo, M., Maggini, M., Marchese, S., Messina, D., Monaco, C., and Naso, S.: Brief communication: Co-seismic displacement on 26 and 30 October 2016 (Mw = 5.9 and 6.5) – earthquakes in central Italy from the analysis of a local GNSS network, Nat. Hazards Earth Syst. Sci., 17, 1885–1892, https://doi.org/10.5194/nhess-17-1885-2017, 2017.

Dewey, J. F., Helman, S., Knott, D., Turco, E. and Hutton, D. H. W.: Kinematics of the western Mediterranean, Geological
425 Society, London, Special Publications, 45, 265-283, https://doi.org/10.1144/GSL.SP.1989.045.01.15, 1989.

Dietrich, J. T.,:Applications of structure-from-motion photogrammetry to fluvial geomorphology, PhD Thesis, 2014.

Dietrich, J. T.: Bathymetric Structure-from-Motion: extracting shallow stream bathymetry from multi-view stereo photogrammetry, Earth Surf. Proc. Land., 42, 355–364, https://doi.org/10.1002/esp.4060, 2016/a.

Dietrich, J. T.: Riverscape mapping with helicopter-based Structure from-Motion photogrammetry, Geomorphology, 252,
430 144–157, https://doi.org/10.1016/j.geomorph.2015.05.008, 2016/b.

Eltner, A, Baumgart, P, Maas, HG, Faust, D.: Multi-temporal UAV data for automatic measurement of rill and interrill erosion on loess soil, Earth Surface Processes and Landforms 40: 741–755, DOI:10.1002/esp.3673, 2015.

Fonstad, M. A., Dietrich, J. T., Courville, B C., Jensen, J. L., Carbonneau, P. E.: Topographic Structure from Motion: A New Development in Photogrammetric Measurement, Earth Surface Processes and Landforms 38 (4): 421–430,
435 doi:10.1002/esp.3366, 2013.

Fugazza, D., Scaioni, M., Corti, M., D'Agata, C., Azzoni, R. S., Cernuschi, M., Smiraglia, C., and Diolaiuti, G. A.: Combination of UAV and terrestrial photogrammetry to assess rapid glacier evolution and map glacier hazards, Nat. Hazards Earth Syst. Sci., 18, 1055–1071, https://doi.org/10.5194/nhess-18-1055-2018, 2018.

Geoscience Australia: http://www.ga.gov.au/earthmonitoring/geodesy/auspos-online-gps-processingservice.html , 2011.

440 Gomez, C., Purdie, H.: UAV- based Photogrammetry and Geocomputing for Hazards and Disaster Risk Monitoring, Geoenviron Disasters 3, 23, https://doi.org/10.1186/s40677-016-0060-y, 2016.

Gomez-Gutierrez, A., Schnabel, S., Berenguer-Sempere, F., Lavado-Contador, F., Rubio-Delgado, J.: Using 3D photo-reconstruction methods to estimate gully headcut erosion, Catena 120: 91–101, DOI:10.1016/j.catena.2014.04.004, 2014.

Giordan, D., Manconi, A., Remondino, F. & Nex, F.: Use of unmanned aerial vehicles in monitoring application and
445 management of natural hazards, Geomatics, Natural Hazards and Risk, 8:1, 1-4, DOI:10.1080/19475705.2017.1315619, 2017.

Harwin, S., Lucieer, A.: Assessing the Accuracy of Georeferenced Point Clouds Produced via Multi-View Stereopsis from Unmanned Aerial Vehicle (UAV) Imagery, Remote Sensing 4 (6): 1573–1599, doi:10.3390/rs4061573, 2012.

Heindel, R. C., Chipman, J. W., Dietrich, J. T., and Virginia, R. A.: Quantifying rates of soil deflation with Structure-from-
450 Motion photogrammetry in west Greenland, Arct. Antarct. Alp. Res., 50, SI00012, https://doi.org/10.1080/15230430.2017.1415852, 2018.

Immerzeel, W., Kraaijenbrink, P., and Andreassen, L.: Use of an Unmanned Aerial Vehicle to assess recent surface elevation change of Storbreen in Norway, The Cryosphere Discuss., https://doi.org/10.5194/tc-2016-292, 2017.

INGV: Comunicato sull'eruzione di fango in C.da Terrapelata-Santa Barbara (Cl) 11 Agosto 2008 — Aggiornamento del 16
455   Agosto, Istituto Nazionale di Geofisica e Vulcanologia, Sezione di Palermo (2008), (availble at http://www.pa.ingv.it/),
2008.

Jalandoni, A., Domingo, I., and Taçon, P. S. C.: Testing the value of low-cost structure-from-motion (SfM) photogrammetry
for metric and visual analysis of rock art, Journal of Archaeological Science: Reports, 17, 605–616,
https://doi.org/10.1016/j.jasrep.2017.12.020, 2018.

460   James, M.R., Robson, S.: Sequential digital elevation models of active lava flows from ground-based stereo time-lapse
imagery, ISPRS Journal of Photogrammetry and Remote Sensing 97: 160–170, DOI:10.1016/j.isprsjprs.2014.08.011,
2014/b.

James, M.R., Varley, N.: Identification of structural controls in an active lava dome with high resolution DEMs: Volcán de
Colima, Mexico, Geophysical Research Letters 39: L22303, DOI:10.1029/ 2012GL054245.L22303, 2012.

465   James, M. R., and Robson, S.: Straightforward Reconstruction of 3D Surfaces and Topography with a Camera: Accuracy
and Geoscience Application, Journal of Geophysical Research: Earth Surface 117 (3): 1–17, doi:10.1029/2011JF002289,
2012.

James, M. R., Robson, S., Smith, M.W.: 3-D uncertainty-based topographic change detection with structure-from-motion
photogrammetry: precision maps for ground control and directly georeferenced surveys, Earth Surf. Proc. Landforms,
470   doi:10.1002/esp.4125, 2017/b.

James, M. R., Robson, S., d'Oleire-Oltmanns, S., Niethammer, U.: Optimising UAV topographic surveys processed with
structure-from-motion: Ground control quality, quantity and bundle adjustment, Geomorphology, Volume 280, Pages 51-66,
ISSN 0169-555X, doi.org/10.1016/j.geomorph.2016.11.021, 2017/a.

James, M. R.: SfM-MVS PhotoScan image processing exercise, IAVCEI 2017 UAS workshop: Lancaster University, 2017.

475   Javernick, L., Hicks, D.M., Measures, R., Caruso, B., Brasington, J.: Numerical modelling of braided rivers with structure-
from-motion derived terrain models, River Research and Applications 32: 1071–1081, DOI:10.1002/rra.2918, 2016.

Javernick, L., Brasington, J., Caruso, B.: Modeling the topography of shallow braided rivers using Structure-from-Motion
photogrammetry, Geomorphology, Volume 213, Pages 166-182, ISSN 0169-555X,
https://doi.org/10.1016/j.geomorph.2014.01.006, 2014.

480   Jia, M., Dawson, J.: AUSPOS: Geoscience Australia's online GPS positioning service, 27th International Technical Meeting
of the Satellite Division of the Institute of Navigation, ION GNSS 2014, 1. 315-320, 2014.

Johnson, K., Nissen, E., Saripalli, S., Arrowsmith, J. R., McGarey, P., Scharer, K., Williams, P., Blisniuk, K.: Rapid
mapping of ultrafine fault zone topography with structure from motion, Geosphere ; 10 (5): 969–986, doi:
https://doi.org/10.1130/GES01017.1, 2014.

485   Kaab, A.: Photogrammetry for early recognition of high mountain hazards: New techniques and applications, Physics and
Chemistry of the Earth, Part B: Hydrology, Oceans and Atmosphere, Volume 25, Issue 9, Pages 765-770, ISSN 1464-1909,
https://doi.org/10.1016/S1464-1909(00)00099-X, 2000.

Kendra, J., Nissen, E., Saripalli, S., Arrowsmith, J.R., P McGarey, P., Scharer, K., Williams, P., Blisniuk, K.: Rapid Mapping of Ultrafine Fault Zone Topography with Structure from Motion, Geosphere 10 (5): 969–986, doi:10.1130/GES01017.1, 2014.

490

Lague, D., Brodu, N., Leroux, J.: Accurate 3D comparison of complex topography with terrestrial laser scanner: application to the Rangitikei canyon (N-Z), ISPRS Journal of Photogrammetry and Remote Sensing 82: 10–26, DOI:10.1016/j.isprsjprs.2013.04.009, 2013.

Lickorish, W. H., Grasso, M., Butler, R. W. H., Argnani, A., and Maniscalco, R.: Structural styles and regional tectonic

495 setting of the "Gela Nappe" and frontal part of the Maghrebian thrust belt in Sicily, Tectonics, 18, 655–668, 1999,

Lucieer, A., de Jong, S.M., Turner D.: Mapping landslide displacements using Structure from Motion (SfM) and image correlation of multi-temporal UAV photography, Progress in Physical Geography 38: 97–116, DOI:10.1177/0309133313515293, 2014.

Madonia, P., Grassa, F., Cangemi, M., and Musumeci, C.: Geomorphological and geochemical characterization of the 11

500 August 2008 mud volcano eruption at S. Barbara village (Sicily, Italy) and its possible relationship with seismic activity, Nat. Hazards Earth Syst. Sci., 11, 1545–1557, https://doi.org/10.5194/nhess-11-1545-2011, 2011.

Marteau, B., Vericat, D., Gibbins, C., Batalla, R. J., and Green, D. R.: Application of Structure-from-Motion photogrammetry to river restoration, Earth Surf. Proc. Land., 42, 503–515, https://doi.org/10.1002/esp.4086, 2016.

Mercer, J. J. and Westbrook, C. J.: Ultrahigh-resolution mapping of peatland microform using ground-based structure from

505 motion with multiview stereo, J. Geophys. Res.-Biogeo., 121, 2901–2916, https://doi.org/10.1002/2016JG003478, 2016.

Monaco, C. and Tortorici, L.: Clay diapirs in Neogene-Quaternary sediments of central Sicily: evidence for accretionary processes, J. Struct. Geol., Volume 18, Issue 10, Pages 1265-1269, ISSN 0191-8141, https://doi.org/10.1016/S0191-8141(96)00046-6, 1996.

Morgan, J. A., Brogan, D. J., and Nelson, P. A.: Application of Structure-from-Motion photogrammetry in laboratory

510 flumes, Geomorphology, 276, 125–143, https://doi.org/10.1016/j.geomorph.2016.10.021, 2017.

Niethammer, U., James, M., Rothmund, S., Travelletti, J., and Joswig, M.: UAV-based remote sensing of the Super-Sauze landslide: Evaluation and results, Eng. Geol., 128, 2–11, https://doi.org/10.1016/j.enggeo.2011.03.012, 2012.

Pearson, E., Smith, M., Klaar, M., and Brown, L..: Can high resolution 3-D topographic surveys provide reliable grain size estimates in gravel bed rivers?, Geomorphology, 293, 143–155, https://doi.org/10.1016/j.geomorph.2017.05.015, 2017.

515 Piermattei, L., Carturan, L., de Blasi, F., Tarolli, P., Dalla Fontana, G., Vettore, A., and Pfeifer, N.: Suitability of ground-based SfMMVS for monitoring glacial and periglacial processes, Earth Surf. Dynam., 4, 425–443, https://doi.org/10.5194/esurf-4-425-2016, 2016.

Prosdocimi, M., Burguet, M., Di Prima, S., Sofia, G., Terol, E., Comino, J. R., Cerdà, A., and Tarolli, P.: Rainfall simulation and Structure-from-Motion photogrammetry for the analysis of soil water erosion in Mediterranean vineyards, Sci. Total

520 Environ., 574, 204–215, https://doi.org/10.1016/j.scitotenv.2016.09.036, 2017.

Regione Siciliana: Emergenza "Maccalube" dell'11 Agosto 2008 nel Comune di Caltanissetta,Descrizione dell'evento e dei danni, Regione Siciliana, Presidenza, Dipartimento della Protezione Civile, Servizio di Caltanissetta, Settembre 2008, p. 30 report available at: http://www.regione.sicilia.it/presidenza/protezionecivile/documenti/documenti.asp, 2008.

Russell, T. S.: Calculating the Uncertainty of a Structure from Motion (SfM) Model, Cadman Quarry, Monroe, Washington,
525   University of Washington report available at: https://digital.lib.washington.edu/researchworks/bitstream/handle/1773/36262/ Russell_MESSAGeReport030.pdf?sequence=1&isAllowed=y, 2016.

Ryan, J.C., Hubbard, A.L., Box, J.E., Todd, J., Christoffersen, P., Carr, J.R., Holt, T.O., Snooke, N.: UAV photogrammetry and structure from motion to assess calving dynamics at Store Glacier, a large outlet draining the Greenland ice sheet, The Cryosphere 9: 1–11, DOI:10.5194/tc-9-1-2015, 2015.

530   Sapirstein, P. and Murray, S.: Establishing Best Practices for Photogrammetric Recording During Archaeological Fieldwork, J. Field Archaeol., 42, 337–350, https://doi.org/10.1080/00934690.2017.1338513, 2017.

Sapirstein, P.: Accurate measurement with photogrammetry at large sites, J. Archaeol. Sci., Volume 66, Pages 137-145, ISSN 0305-4403, https://doi.org/10.1016/j.jas.2016.01.002, 2016.

Sapirstein, P.: A high-precision photogrammetric recording system for small artifacts, J. Cult. Herit., 31, 33–45,
535   https://doi.org/10.1016/j.culher.2017.10.011, 2018.

Seitz, L., Haas, C., Noack, M., and Wieprecht, S.: From picture to porosity of river bed material using Structure-from-Motion with Multi-View-Stereo, Geomorphology, 306, 80–89, https://doi.org/10.1016/j.geomorph.2018.01.014, 2018.

Serpelloni, E., Vannucci, G., Pondrelli, S., Argnani, A., Casula, G., Anzidei, M., Baldi, P., Gasperini, P.: Kinematics of the Western Africa-Eurasia plate boundary from focal mechanisms and GPS data, Geophysical Journal International, Volume
540   169, Issue 3, June 2007, Pages 1180–1200, https://doi.org/10.1111/j.1365-246X.2007.03367.x, 2007.

Smith, M.W., Quincey, D.J., Dixon, T., Bingham, R.G., Carrivick, J.L., Irvine- Fynn, T.D.L., Rippin, D.M.: Aerodynamic roughness of glacial ice surfaces derived from high-resolution topographic data, Journal of Geophysical Research - Earth Surface 121: 748–766, DOI:10.1002/ 2015jf003759, 2016.

Smith, M.W. and Vericat, D.: From experimental plots to experimental landscapes: topography, erosion and deposition in
545   sub-humid badlands from Structure-from-Motion photogrammetry, Earth Surf. Proc. Land., 40, 1656–1671, https://doi.org/10.1002/esp.3747, 2015.

Snapir, B., Hobbs, S., and Waine, T.: Roughness measurements over an agricultural soil surface with Structure from Motion, ISPRS J. Photogramm., 96, 210–223, https://doi.org/10.1016/j.isprsjprs.2014.07.010, 2014.

Tahar, K. M.: An evaluation on different number of ground control points in unmanned aerial vehicle photogrammetric
550   block, ISPRS - International Archives of the Photogrammetry, Remote Sensing and Spatial Information Sciences, XL-2/W2. 93-98. 10.5194/isprsarchives-XL-2-W2-93-2013, 2013.

USGS: Unmanned Aircraft Systems Data Post-Processing, United States Geological Survey, UAS Federal Users Workshop 2017, https://uas.usgs.gov/pdf/PhotoScanProcessingDSLRMar2017.pdf, consulted at 30 of May2018, 2017.

Vinci, A., Todisco, F., Brigante, R., Mannocchi, F., and Radicioni, F.: A smartphone camera for the structure from motion

555   reconstruction for measuring soil surface variations and soil loss due to erosion, Hydrol. Res., 48, 673–685, https://doi.org/10.2166/nh.2017.075, 2017.

Westoby, M.J., Brasington, J., Glasser, N.F., Hambrey, M.J., Reynolds, J.M., Hassan, M.A.A.M., Lowe, A.: Numerical modelling of glacial lake outburst floods using physically based dam-breach models, Earth Surface Dynamics 3: 171–199, DOI:10.5194/esurf-3-171-2015, 2015.

560   Westoby, M. J., Brasington, J., Glasser, N. F., Hambrey, M. J. and Reynolds, J. M.: Structure-from-Motion Photogrammetry: A Low-Cost, Effective Tool for Geoscience Applications, Geomorphology 179, Elsevier B.V.: 300–314, doi:10.1016/j.geomorph.2012.08.021, 2012.

Woodget, A.S., Carbonneau, P.E., Visser, F., Maddock, I.P.: Quantifying submerged fluvial topography using hyperspatial resolution UAS imagery and structure from motion photogrammetry, Earth Surface Processes and Landforms 40: 47–64,

565   DOI:10.1002/esp.3613, 2015.